ACS Energy LETTERS

http://pubs.acs.org/journal/aelccp

LETTER

Direct Measurement of Electrochemical Selectivity Gradients over a 25 cm^2 Copper Gas Diffusion Electrode

Hunter Simonson, Walter Ellis Klein, Danielle Henckel, Sumit Verma, K. C. Neyerlin, and Wilson A. Smith*

Cite This: *ACS Energy Lett.* 2023, 8, 3811−3819

Read Online

ACCESS | Metrics & More | Article Recommendations | Supporting Information

ABSTRACT: Electrochemical CO reduction (COR) systems have increased by orders of magnitude in their accessible activities in the past decade, particularly by the implementation of the gas diffusion electrode (GDE) architecture. As GDEs are upscaled by active geometric area (cm^2 to m^2), reactor performance can change due to physical and chemical spatial variations which are complicated by the chemical complexity of multiphase and multiproduct electrochemical systems. This work measures and evaluates COR performance metrics by a multiport sampling reactor to measure reactant and product concentration down-the-channel of a COR GDE. It is found that the faradaic efficiency (FE) toward the hydrogen evolution reaction (HER) increases down-the-channel, largely driven by a decrease in the partial pressure of CO, while the selectivity for ethylene remains relatively constant down-the-channel. This work highlights the inhomogeneities in performance as electrochemical reactors are physically upscaled and has significant implications for future scaling of COR and CO2R systems.

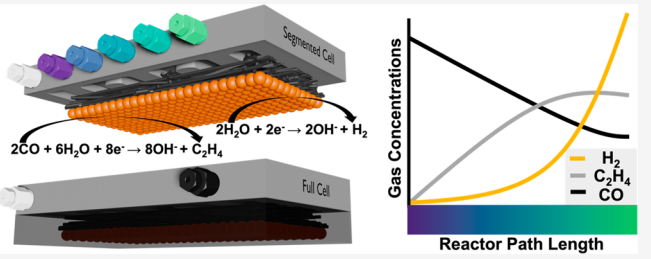

Rapidly increasing levels of carbon dioxide (CO_2) in the atmosphere due to human activities are poised to cause irreparable damage to the earth's climate without technological innovation and intervention.[1] Carbon capture and utilization will play a crucial role in achieving a net-zero carbon emissions future as outlined in the Paris Agreement. The electrochemical reduction of CO_2 (CO2R) and the electrochemical reduction of CO (COR) are maturing technologies which hold promise for making chemical feedstocks from captured carbon emissions and renewable electricity at economically appealing rates.[2−4] In recent years, COR has gained considerable attention due to its unique reactant utilization, equilibration with electrolytes, and product spectrum, which differ considerably from those of CO2R, which allows for its own independent understanding, optimization, and technological value chain.[5] Researchers have innovated catalyst development, electrode design, and reactor architecture sufficiently to achieve performance benchmarks for reactor size (400 cm^2), stability (500 h), electrode activity (2.5 A-cm^{-2}), product selectivity (80%), and reactant single pass conversion (84%) to justify exploring deployment of pilot plant-scale technologies.[6−9] While these performance metrics were achieved in independent systems, achieving them together in a large, stable, selective, and active electrochemical reactor remains a challenging task.

As COR electrochemical reactors are increased in physical and energetic scale to achieve higher overall reaction rates, reactant utilization, quantified by the single pass conversion (SPC) becomes uniquely important to the overall cost of operation as well as system performance.[10−13] Translating state-of-the-art electrochemical reactor performance from the lab-scale to pilot-scale is not as facile as increasing the reactant conversion, as at reactor sizes beyond the benchtop scale previously negligible effects such as heat accumulation, flow pressure and velocity, water management, and current distributions can become dominant in driving local reaction activity and selectivity. To better understand the reaction activity and selectivity within an electrolyzer, it is essential to experimentally deconvolute these synergistic variables that influence scalability within an operating reactor.

One method to accomplish this is to partition the reactor into subunits that can measure individually quantifiable data

Received: July 20, 2023
Accepted: August 16, 2023
Published: August 21, 2023

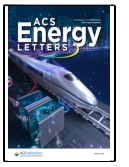

https://doi.org/10.1021/acsenergylett.3c01489
ACS Energy Lett. 2023, 8, 3811−3819

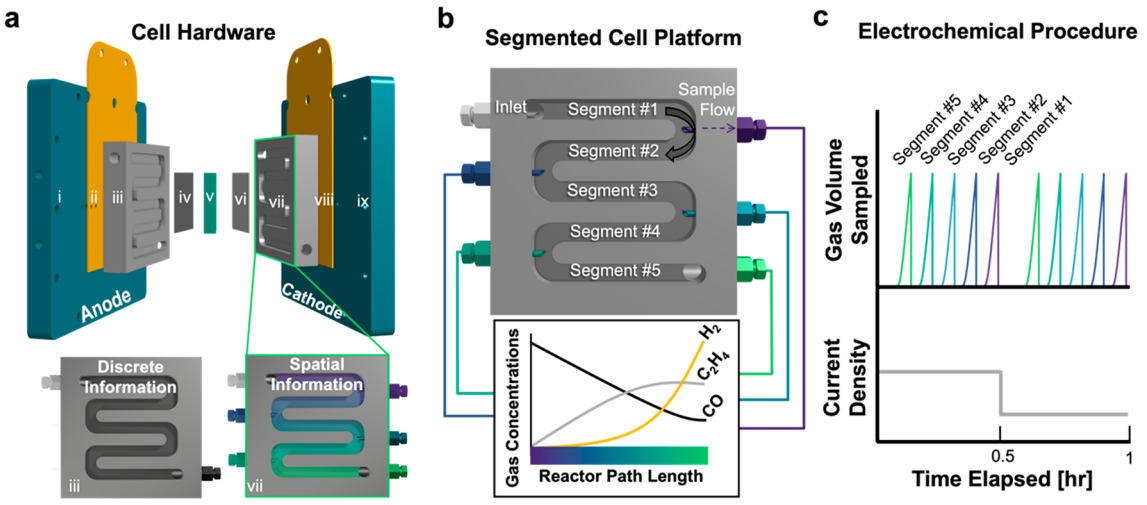

Figure 1. Schematic of segmented cell used for spatial compositional measurements. (a) Depiction of typical reactor testing hardware, in sequential order: i. Anode compression plate, ii. Anode current distributor, iii. Anode flow field, iv. Anode porous transport layer, v. Anion vc fxd exchange membrane vi. Cathode GDE vii. Cathode flow field, viii. Cathode current distributor, ix. Cathode compression plate. Beneath the hardware blowout is a depiction of the gas sampling adaption to the cathode flow field, which encompasses the segmented cell. (b) Depiction of the segmented cell flow field (with 1 channel instead of 10 for simplicity), with insets showing the compositional information that can be collected in each 5 cm^2 increment of the 25 cm^2 active geometric area and a representation of the increased dimensionality available for compositional measurement. (c) Sampling scheme to collect a segmented polarization curve, where a constant current density is applied and the gas composition is iteratively sampled along the reactor, from outlet to inlet.

which can break down the performance of the ensemble reactor into the performance of its constituent components.[14,15] This method, referred to as a segmented cell, has been used extensively in fuel cells, water electrolysis, and flow batteries to simulate the performance of a larger electrochemical reactor by mapping performance as a function of reactor size in a lab scale reactor, and translating the results to develop direct process intensification scaling relations.[16−18] Reactor segmentation offers a unique platform to study COR electrolysis at scale, as the partitioned system will have additional changes along its component segments due to the product selectivity of COR being less than unity as opposed to water electrolysis. Initial works have examined the effects of simulated reactant distributions, humidity, and thermal gradients on similar chemistries.[19−21] Crucially though, the relationship between reactant conversion, reaction selectivity, and electrode size has yet to be established for COR systems.

To probe these correlated parameters, we designed and implemented an augmented flow field to allow for operando sampling of the concentrations of cathodic gas stream products and reactant ver a gas diffusion electrode.[22,23] The segmented cell platform allows for direct measurement of gas compositions as a function of geometric electrode area, which can be converted to reaction conversion and selectivity at individual segments within the reactor under various reaction conditions. To highlight the platform's capabilities and elucidate scaling pathways for COR, electrochemical tests were performed with the segmented cell performing COR, with the major product formed being ethylene (C_2H_4). This tool provides a unique window to examine the performance of a GDE based electrolyzer, and the technology can be easily translated to analogous chemistries such as CO2R, liquid fed MEAs, or complimented with additional analytical techniques.

A multichannel flow field was modified to accept sampling ports at each bend in the serpentine pattern of the flow field design.[22,24] The flow field is a 10 channel (0.5 mm land and channel width, 0.833 mm channel depth), five-pass serpentine design (Figures S1−S2) comprising a total active area of 25 cm^2. The sampling ports were located at each bend in the serpentine pattern of the 10 channels, such that each port sampled the gas stream after passing over 5 cm^2 of the electrode area, effectively compartmentalizing the 25 cm^2 electrode into five distinct and sequential segments. The selected small dimensions (0.5 mm width/0.833 mm depth) of the 10 serpentine channels of the flow field ensure a homogeneous distribution of reactant among each segment,[25] allowing this system to track the reaction conversion and selectivity down the length of the reactor in regular intervals. A representation of the electrochemical testing hardware and modifications made to the cathode flow field to enable segmented operation is shown in Figure 1a. A depiction of the segmented sampling scheme, along with representative concentration data, is shown in Figure 1b. To probe the COR reaction, the cathode in all experiments consisted of copper nanoparticles dispersed in Nafion coated onto a Sigracet 39BB gas diffusion layer operated in a zero-gap arrangement, with an Ionomr Aemion 15 μm anion exchange membrane (AEM) as the separator from a titanium felt anode coated with IrO_2 and a perfluorinated anion exchange polymer which was produced internally,[26] over which 1 M KOH was recirculated. All electrochemical COR experiments were conducted with a cathode feed of 95% relative humidity (RH) and held at 60 °C. Reaction performance was quantified by the Faradaic efficiency (FE) (Supplementary eq 2 - ES2), which is the electrochemical analogue to selectivity, the partial current density (J_i) (ES4) toward the two main electrochemical products (H_2, C_2H_4), which is the electrochemical analogue to reaction rate, and the SPC of the COR reaction (ES5).

SINGLE PASS CONVERSION AND REACTION SELECTIVITY DOWN-THE-CHANNEL

First, the effect of the CO flow rate and subsequent SPC on the selectivity for COR was examined for the full 25 cm^2

https://doi.org/10.1021/acsenergylett.3c01489
ACS Energy Lett. 2023, 8, 3811−3819

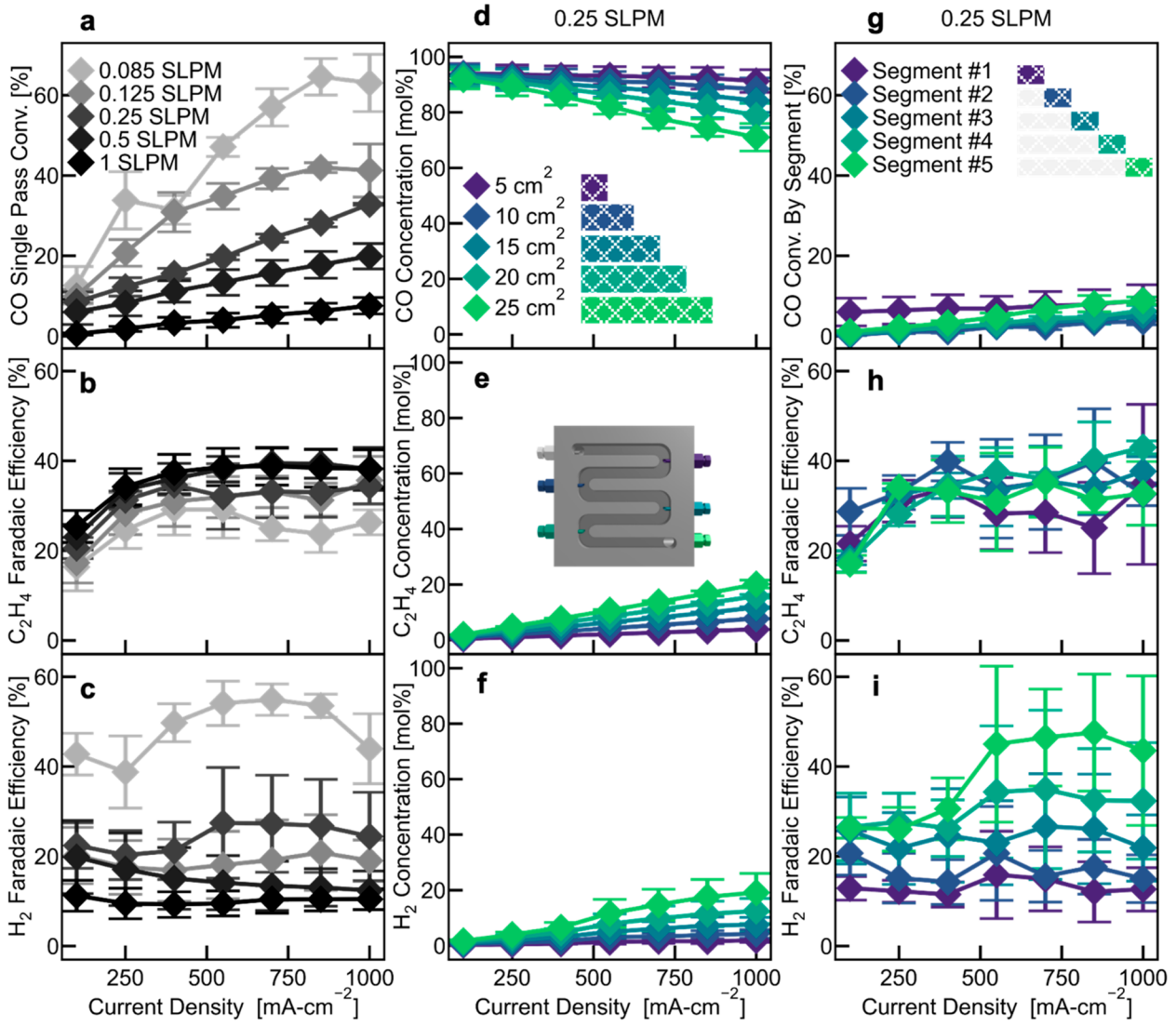

Figure 2. Effect of reactant flow rate on reactor performance and down-the-channel analysis. (a−c) Single pass conversion efficiency of the CO reactant and faradaic efficiencies toward ethylene and hydrogen, respectively, collected with the 25 cm^2 electrode at multiple inlet flow rates of CO. (d,e,f) Slice of the data in (a,b,c) respectively, at 0.25 SLPM, expanded using the segmented cell platform, with the same data now plotted for each iteratively larger electrode area over which the data was collected, plotted as each individual gas concentration. (g,h,i) Slice of the data in (a,b,c) respectively, at 0.25 SLPM expanded using the segmented cell platform, with the segment-wise single pass conversion (g) and faradaic efficiencies toward ethylene and hydrogen (h,i) now being plotted for each individual electrode segment where the data was collected. Lines are added to guide the eye. Insets in panel (d) and (g) are given which show the difference between area-normalization and segment-normalization.

reactor as the current density of the system was increased in regular intervals up to 1 A-cm^{-2}. The inlet flow rate of CO was decreased from 1.0 to 0.5, 0.25, 0.125, and 0.085 SLPM in individual experiments, each at 95% RH. The backpressure was controlled in the reactor to maintain a constant CO inlet partial pressure of 1 bara, which ensures no backflow from later segments to prior segments (Figures S24, S26). Current holds were performed at 100, 250, 400, 550, 700, 850, and 1000 mA-cm^{-2} for 30 min each to collect the reactant and product distribution at each sampling point, as shown in Figure 1c. The resultant single pass conversion is shown in Figure 2a, and the faradaic efficiency toward C_2H_4 and H_2 are shown in Figure 2b and 2c for the discrete 25 cm^2 system. Overall, it was observed that the SPC for COR and the FE toward H_2 increased with decreasing flow rate. However, between the highest flow rate and lowest flow rate, the selectivity for ethylene exhibited a slight decrease in FE while the increase in FE toward H_2 increased significantly (>50%) across the flow rates measured. Utilizing the segmented cell, one flow condition from Figure 2a−c can be isolated and expanded to show the concentrations of products at each sampling point, functionally measuring the concentrations for each iteratively larger electrode area, as shown in Figure 2d−f for the 0.25 SLPM condition. By converting the concentrations were converted into faradaic efficiencies and the performance was subtracted from the prior sampling point (shown schematically in Figure S3), the faradaic efficiency for each sequential 5 cm^2 segment can be calculated and compared, as shown for 0.25 SLPM in Figure 2g−i. Normalizing reactor performance by segment increases the uncertainty in the FE's due to error propagation from one segment to the next; however, it also emphasizes down-the-channel trends, and segment-normalization allows each reactor

https://doi.org/10.1021/acsenergylett.3c01489
ACS Energy Lett. 2023, 8, 3811−3819

segment to be treated as an individual 5 cm^2 reactor with a unique feed composition. An expanded breakdown of the segmented cell data covering all operational conditions and normalizations can be found in Figures S3−S9. Isolating the reaction selectivity for each individual segment within the electrolyzer shows that the faradaic efficiency toward ethylene remains relatively constant along the length of the reactor (Figure 2h). This trend holds true except in conditions causing high SPC, such as at very low flow rates or moderate flow rates combined with high current densities. Conversely, the H_2 FE increases down-the-channel with the electrode segment in all cases observed. The magnitude of H_2 FE increases down-the-channel is larger than the decreases of the ethylene FE (Figure S10), showing that there must be a compensatory decrease in other COR products, such as ethanol, propanol, and acetate. Additionally, it is unlikely that these effects are purely driven by inhomogeneities in copper loadings, differences in water vapor partial pressure between experiments due to humidity, or voltametric effects, as these have been separately measured and accounted for (Figures S25, S27, S29).

A potential cause for the observed increase in H_2 FE down-the-channel could be due to kinetic or transport limitations driven by a decrease in the partial pressure of reactant CO. As the reaction proceeds along the reactor, the feed stream becomes diluted with H_2 and the pressure drops in the flow field due to the loss of reactant from electrochemical conversion. To decouple the effects of reactor flow path and CO partial pressure, a series of dilution experiments were performed using a similar range of CO flow rates as in Figure 2, while diluting the reactor feed stream with N_2 until a total feed flow rate of 1 SLPM was achieved, resulting in dry CO inlet molar concentrations of 8.5%, 12.5%, 25%, 32.5%, 50%, 75%, and 100% CO, all with a total feed gas flow rate of 1 SLPM. The flow dilution data set is plotted in Figure 3a−c and

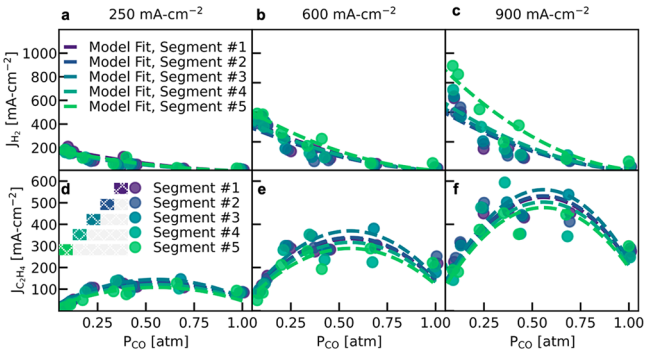

Figure 3. Effect of CO partial pressure on main product partial current densities. (a−c) Partial current density toward hydrogen at 250, 600, and 900 mA-cm^{-2}, respectively, plotted versus the partial pressure of CO [atm] present in each respective segment's flow channels, with the results of a microkinetic fit plotted as dashed lines. (d−f) Partial current density toward ethylene at the same conditions as panels (a−c). Inset in panel (d) shown to emphasize the segment-specific normalization used.

3d−f as the partial current density of H_2 and C_2H_4 for each individual segment versus the average partial pressure of CO in that segment, respectively. Full dilution data across a larger range of current densities can be found in Figure S38, as well as Figures S36−S37, S39−S40, for different model parameters. Expectedly, the hydrogen partial current density increases with decreasing CO partial pressure, while the partial current density toward ethylene exhibits a parabolic relationship with CO partial pressure, peaking between 0.4 and 0.6 atm_{CO}. These relationships can be understood by applying a microkinetic model using the COR rate limiting steps, with the model fit plotted for each current density and segment in Figure 3. The details of the microkinetic model can be found in ES33−ES40, which fits the partial current densities of hydrogen and ethylene to a second order dependence on the surface coverage of water, and a first order dependence on the surface coverage of water and CO, respectively.[27] The surface coverages of both water and CO can be calculated from the partial pressure of CO after accounting for the hydrophobicity of surface-bound CO, shown in Figure S30.[27,28] Solving for the potential dependent rate constants at each current, the trends in the partial current densities are well-captured by the model, for which the resultant data fit is plotted as dashed lines in Figure 3. The model yields good agreement with the dilution data for 250, 500, 600, 700, 800, 900, and 1000 mA-cm^{-2}, as evident by the coefficient of determination for each model fit given in Table S2. Down-the-channel trends are still present in the dilution data set (Figures S11−S14) shown in Figure 3c; however, they are less pronounced than in the pure-feed COR experiments. Significant differences in electrochemical performance between the first and fifth 5 cm^2 segments still exist after accounting for the partial pressure differences, particularly at the higher current densities in Figure 3, shown by the variability in the resultant rate constants from the microkinetic model (Figures S31−S35).

The dilution experiments can serve to better understand the influence of the CO concentration on the reaction FE, as a lower CO concentration can be achieved without having a high SPC. A statistical resampling method was applied to the combined data collected from Figures 2 and 3 to further separate the effects of reactant concentration and conversion. In this method, key independent variables were identified (CO concentration, SPC, reactant stoichiometric coefficient, S29), HER partial current density, and non-C_2H_4 J_{COR} (ES30)) and five partitions of the total data set from Figures 2 and 3 were taken, with each partition being relatively constant in one of the analyzed independent variables (varying by less than 1% of its total range of measurement), shown in Figure S15A. Then, the influence of each of the other independent variables on H_2 and C_2H_4 FE can be determined for the partition of the data set where one independent variable is constant. An example of one iteration in this method would be to look at the influence of CO concentration on H_2 and C_2H_4 FE over a region in the combined data set where CO SPC varies by less than 1% of the total range of SPC data (Figure S15B−F). After accounting for the covariances between independent variables, the clearest trend observed is that the FE toward H_2 increases with decreasing CO concentration in every case (Table S3), which is consistent with the results shown in Figure 3. Similarly, the FE toward C_2H_4 decreases with increasing H_2 partial current density. This relationship is likely not solely an inversely proportional one, i.e., *not* just C_2H_4 FE decreasing as HER increases, as this relationship holds true even at a constant single pass conversion (Figure S15D,xi), implying that regions of high HER could be further influencing the local reaction conditions as the reaction proceeds along the reactor. Further insights are needed to examine this hypothesis, and future experiments will be necessary to better decouple these competing effects, which may be causing selectivity gradients as reactor areas increase.

https://doi.org/10.1021/acsenergylett.3c01489
ACS Energy Lett. 2023, 8, 3811−3819

An alternative method is still needed to understand the unexplained decrease in ethylene FE with an increasing H_2 partial current density. The conditions local to the COR active area, i.e., the confluence of reactant CO, buffering electrolyte, and active catalyst material, referred to as the *microenvironment*, could be changing independent of or in concert with the prior observed process variables, causing the decrease of C_2H_4 FE with increasing H_2 partial current density. While electrochemical techniques exist to probe characteristics at electrodes surfaces, observing down-the-channel potential or current trends with those techniques would require a more advanced reactor system than is used in this study, and is thus outside the scope of this work. Instead, a limiting current density method used extensively for fuel cell GDEs was adapted to help resolve down-the-channel trends in the COR microenvironment.[29] To accomplish this, the reactant feed stream was set to a flow rate where the reaction will not be stoichiometrically limited, quantified by the *stoichiometric coefficient* (ES29), which is the ratio between the reactant flow rate and the reactant flow rate necessary to achieve 100% SPC at 100% FE toward COR for a specific current density. In these experiments, the inlet reactant streams are sufficiently diluted with N_2 to induce mass transport limitations of the reactant, emulating the limiting current density framework developed in fuel cell technologies.[30] The process is shown schematically in Figure S16, where the feed stream is sufficiently diluted to observe mass transfer effects at an inlet CO concentration of 12.5% and a total gas flow rate of 1 SLPM, with the mass transport effects appearing as limiting partial current densities toward ethylene.

The experimental data from this figure was used in a 1-D mass transport model which simulated the microenvironment of the catalyst along the reactor path length. The details of the transport model can be found in the SI (ES10−26, Table S1, Figure S16−S19). Briefly, the model consists of calculating the concentrations and transport of CO from the channels of the flow field through the GDE to the catalyst surface. Components of the model include molecular and Knudsen diffusion in the gas diffusion layer and microporous layer, followed by dissolution of CO into the electrolyte and subsequent diffusion of the reactant CO through the electrolyte to the catalyst surface. For the limiting current density model, the boundary condition is chosen such that the concentration of CO at the catalyst surface is 0 when the ethylene partial current density is mass transfer limited. The physical properties of the GDE which feed into the model are well-defined except for the diffusion length scale of CO through the electrolyte, which is the parameter for which the transport model will be solved and is shown schematically in Figure 4b. Applying this technique to the segmented system, Figure 4a shows the partial current density toward ethylene for each reactor segment at a feed composition of 12.5 mol % CO and total flow rate of 1 SLPM, where the mass transfer limited current density is taken as the 5-point average of a segment's partial current density toward ethylene between the total applied current densities of 800 and 1000 mA-cm^{-2}. After extrapolating the COR limited current density from the plateaued regime of the COR polarization curve, that limiting electrochemical reaction rate was translated to a limiting transport rate by Faraday's law of electrolysis (ES20). The limiting transport rate was then dissected through the thickness of the electrode by applying the transport model which yielded

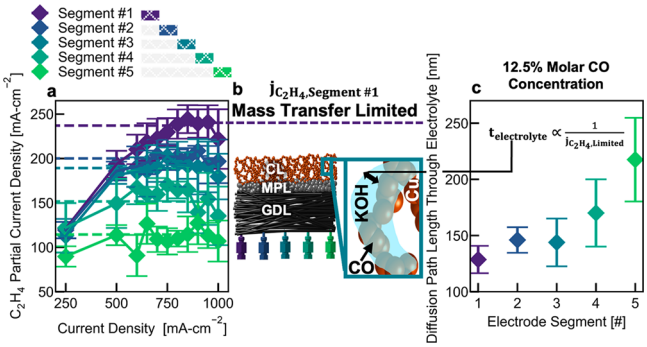

Figure 4. Down-the-channel limiting COR rates and mass transport model interpreted results. (a) Partial current density toward ethylene at a 12.5% CO molar feed for each of the 5 reactor segments. Dotted lines show linear extrapolation of highest 5 current density measurements when the system is in a mass-transfer limited regime. (b) Schematic showing the mass transfer limiting step within the electrode, where CO is diffusing through a representative thin electrolyte film to reach the catalyst surface. (c) Diffusion length scale of CO through electrolyte thin film around the catalyst surface when the COR reaction is mass transfer limited determined by the accompanying transport model, plotted versus electrode segment.

the diffusion length scale through the electrolyte for the reactant CO molecule.

Comparing the calculated diffusion lengths of CO through the electrolyte for segments along the reactor, the diffusional length increases by 71% from the first segment to the fifth segment, from 129 to 221 nm, as shown in Figure 4c. We note that this value, while falling in a reasonable range for electrolyte thin films in porous electrodes,[31] is more qualitative than quantitative as it neglects gaseous diffusion in the catalyst layer, as well as double layer effects to solute diffusivity, which can have a profound impact on gas transport and would likely result in a reduction in the calculated diffusion lengths.[32] Additionally, the description of an electrolyte film is only an interpretation of the results of the transport model, and the diffusion distance could be more accurately described by a flooded agglomerate model with a constant film thickness but an increasing quantity of totally flooded catalyst layer pores down-the-channel, or an amalgamation of the two interpretations.[33] The increase in diffusional transport resistance is indicative of trade-offs between the reaction selectivities toward H_2 and C_2H_4, evident when comparing the relationship between the limiting current model results and the observed selectivity trends down-the-channel in Figure 2. Extensions of the measurement to a wider range of CO concentrations show that the effective diffusion length through the electrolyte increases linearly with the partial current density of the HER, possibly due to bubble-induced surface coverage limitations, or an increased drift factor of flow of products away from the catalyst layer (Figure S17D).[34]

Further potential causes of the observed selectivity gradients in Figure 2 include reactor orientation and pressure distributions inside the flow field. While total gas pressure can certainly influence the performance of the GDE, nominally through reactant partial pressure and the capillary properties of the pores, the change in flow rates between reactor inlet and outlet rarely deviated further than 15% (Figure S23). Still, total flow rate appears to influence the system performance regardless of reactant concentration (Figure S28). The lack

https://doi.org/10.1021/acsenergylett.3c01489
ACS Energy Lett. 2023, 8, 3811−3819

of change in down the channel pressure is due to CO conversion being offset by H_2 production, so it is expected that down-the-channel system pressure effects are negligible for this particular system, but may deviate more significantly for reactors that experience higher rates of reactant consumption.[35] With regard to reactor orientation, the electrodes were operated perpendicular to the earth, with the first segment being the highest and the fifth segment being the lowest in the z plane; however, changing that orientation yields insignificant results (Figure S22). Still, gravitational forces may motivate condensed liquid to accumulate at the end of the reactor, in the fifth segment, causing the observed increase in H_2 production down-the-channel due to electrode flooding. To control for this, two separate experiments were run where the fifth segment of electrode (the final 1 × 5 cm catalyzed region of the GDE) was replaced with either inert material (subgasketed) or uncatalyzed GDL material, respectively. In both cases, the H_2 FE shows similar gradients in HER performance (Figure S20). The results using the uncatalyzed fifth segment experiment indicates the possibility of a nonuniform current density distribution in the full 25 cm^2 electrodes if overpotentials in each segment change, as the apparent current density in the HER-only uncatalyzed GDL is less than the total average applied current density by 40−50% (Figure S21). Despite similar selectivity gradients in smaller electrodes, there is a negative correlation between the amount of non-C_2H_4 products (i.e., liquids: ethanol, acetate, formate) which were produced in subsequent segments and the FE of hydrogen (Table S3), while there is no correlation with the FE of ethylene, highlighting the trade-off between non-C_2H_4 products and hydrogen selectivity. While the presence of liquid hydrocarbons can affect the viscosity of the electrolyte present in the cathode catalyst layer and subsequently the capillary behavior of the catalyst pores, those effects appear to have a negligible influence over the FE of the electrode toward ethylene.[36] Further experiments are needed to better characterize the properties of the catalyst layer microenvironment; however, these experiments provide a facile method to extrapolate down-the-channel properties from a gas diffusion electrode. The proposed cascading cause-and-effect relationship of FE trends observed herein is then i.) The concentration of CO drops due to conversion and dilution by HER, which in turn increases the rate of HER through surface coverage competition (Figure 3a−c), although the dependence of ethylene formation on both surface bound water and CO implies that the increase in HER does not necessarily cause a decrease in ethylene selectivity. Then, (ii) the increased rate of HER modulates the reaction microenvironment, increasing the transport resistance of the reactant CO, and in extreme cases, limits ethylene production by limiting its reactant access and utilization (Figure 4a). This cause-effect relationship is schematically shown in Figure 5. From the first observation in Figure 3, an improved model (ES40−45) can be created which can predict the performance of the CO electrolyzer (Figure S42) and capture the trends mentioned herein without having to hold a process parameter constant (Figure S41).

Overall, there are several recommendations toward future research areas that can be made based on the results shown here. First, as the reactant concentration plays a leading role in driving COR performance, utilizing a flow field design which prioritizes reactant availability and through plane diffusion such as an interdigitated arrangement is recommended.[37] Mediating electrode flooding in the catalyst layer is another important phenomenon to achieve a stable, uniform electrode performance. Analytical tools are needed to better characterize the pore space and electrochemically active regions of a catalyst layer will be necessary to quantify any changes in the actual *operando* catalyst layer saturation, such as the limiting current method shown here or in adjacent techniques.[38] Perforating the microporous layer with structured relief channels is one successful strategy to relieve the liquid accumulation which occurs in the catalyst layer that leads to flooding.[39] Finally, designing the gas diffusion electrode architecture to reduce gas transport resistances may address many of the problems described above.[40] As CO surface coverages are already low in this system, using polymer or ionomer binders to modulate the surface accessible CO is a promising strategy to enhance COR reaction rates and suppress HER increases that occur down-the-reactor.[41,42] Changes in ionomer content and quality to modulate gas transport should be done in the framework of maintaining adequate ion conductivity, especially under dilute molarities of electrolyte. Adding the appropriate polarity and quantity of ionomer to the catalyst layer such that COR catalyst layers have fuel cell-like ion conductivity will be necessary for stable reactor operation with low-conductivity fluids in the anode compartment.[43]

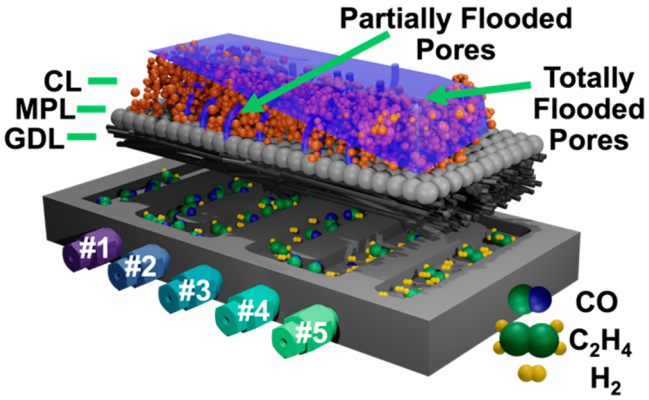

Figure 5. Scheme of key findings utilizing a down-the-channel segmented cell. As the partial pressure of the reactant decreases due to product formation and reactant conversion, the FE toward H_2 increases, causing an increase in transport resistance. Here, the transport resistance is mathematically and schematically interpreted as an increase in the amount of flooding down-the-channel.

Measurement of gas compositions within an electrochemical COR reactor is vital because there are intimately related variables that can influence the selectivity of the reaction as the physical size of the reactor increases and thus directly impacts the performance and scalability of the COR system. Utilizing the segmented cell platform, the effects of reactor path length, reactant partial pressure, and reactant conversion were explicitly quantified and delineated, showing that hydrogen increases down-the-channel due to a decrease in CO partial pressure, verified by a microkinetic model. A limiting current method was developed and implemented which confirmed that the transport resistance for CO was increasing down-the-channel, which can limit COR performance. These results help to form a design framework for improved COR electrodes and reactors as well as demonstrate a powerful analytical tool for surveying the scalability of electrochemical flow systems. Analogous chemistries such as CO2R on an array of catalysts will have different dependencies on reactant concentration due

https://doi.org/10.1021/acsenergylett.3c01489
ACS Energy Lett. 2023, 8, 3811−3819

to the formation of carbonate salts; however, those effects will likely exacerbate the results shown here. Future works will aim to fold in more advanced diagnostic systems to the segmented cell architecture to perform more robust and flexible electrochemical measurements and develop scalable relations between reactant feed quality and reactor size for electrochemical COR.

■ ASSOCIATED CONTENT

Supporting Information

The Supporting Information is available free of charge at https://pubs.acs.org/doi/10.1021/acsenergylett.3c01489.

Experimental procedures for electrochemical experiments, electrode fabrication, and details of the segmented sampling procedure and corresponding product and reactant quantification (ES1−9) can be found in the Supporting Information (SI). The limiting current density and mass transport formulation and model (ES10−26) is exhaustively described within the SI, as well as the microkinetic model (ES32−39) and the comparison between single pass conversion models for predicting electrochemical selectivity (ES40−45). Included in the SI are schematics of the segmented cell system (Figure S1−2), and alternative representations of Figure 2 in Figures S3−9, and similar formulations for Figure 3 in Figure S11−14. The data set resampling method is described and shown in Figure S15 and Table S3, and further figures for the limiting current density model are shown in Figures S16−19. Subgasketing experiments are described and shown in Figure S20−21. System validation experiments can be found in the SI in Figure S22−29. Further fitments of the microkinetic model and discussions are provided in Figure S30−40, and the results of the single pass conversion models are shown in Figure S41−42 (PDF)

■ AUTHOR INFORMATION

Corresponding Author

Wilson A. Smith − *Department of Chemical and Biological Engineering and Renewable and Sustainable Energy Institute (RASEI), University of Colorado Boulder, Boulder, Colorado 80303, United States; National Renewable Energy Laboratory, Golden, Colorado 80401, United States;* orcid.org/0000-0001-7757-5281; Email: Wilson.Smith@nrel.gov

Authors

Hunter Simonson − *Department of Chemical and Biological Engineering and Renewable and Sustainable Energy Institute (RASEI), University of Colorado Boulder, Boulder, Colorado 80303, United States; National Renewable Energy Laboratory, Golden, Colorado 80401, United States*

Walter Ellis Klein − *National Renewable Energy Laboratory, Golden, Colorado 80401, United States;* orcid.org/0009-0000-6495-8304

Danielle Henckel − *National Renewable Energy Laboratory, Golden, Colorado 80401, United States*

Sumit Verma − *Shell International Exploration & Production Inc., Houston, Texas 77082, United States;* orcid.org/0000-0001-8365-180X

K. C. Neyerlin − *National Renewable Energy Laboratory, Golden, Colorado 80401, United States;* orcid.org/0000-0002-6753-9698

Complete contact information is available at: https://pubs.acs.org/10.1021/acsenergylett.3c01489

Author Contributions

Conceptualization, E.K., S.V., K.C.N. and W.A.S.; methodology, H.S., D.H. and E.K.; investigation, H.S.; writing, H.S. and W.A.S.; resources, K.C.N. and W.A.S.; supervision, W.A.S.; funding acquisition, K.C.N. and W.A.S.

Funding

This work was authored in part by the National Renewable Energy Laboratory, operated by Alliance for Sustainable Energy, LLC, for the US Department of Energy (DOE) under Contract No. DE-AC36−08GO28308. System development was supported by the Laboratory Directed Research and Development (LDRD) Program at NREL, and experimental work was supported by Shell's New Energies Research and Technology (NERT) Dense Energy Carriers program under agreement No. ACT-18−00038. The views expressed in the article do not necessarily represent the views of the DOE or the U.S. Government. The U.S. Government retains and the publisher, by accepting the article for publication, acknowledges that the U.S. Government retains a nonexclusive, paid-up, irrevocable, worldwide license to publish or reproduce the published form of this work, or allow others to do so, for U.S. Government purposes.

Notes

The authors declare no competing financial interest.

All raw and processed image data generated in this work, including the representative images provided in the manuscript, are available from the corresponding authors on reasonable request.

■ ACKNOWLEDGMENTS

The authors recognize the Energy Systems Integration Facility (ESIF) and its operations team at NREL for enabling this research. The authors also acknowledge Guido Bender for contributions to the conception of the project, Leiming Hu for helpful discussions on experimental methods, Tim Van Cleve for contributions to the setup of some component characterization, Holly Gadpaille for contributions to analytical methodology, Maarten Schellekens, Paul Corbett and Reza Mirshekari for helpful discussions about the work, Huyen Dinh for intellectual contributions to the work, and Fry Intia for marshaling an environment of safety and excellence in the laboratory.

■ REFERENCES

(1) *Climate Change 2022: Impacts, Adaptation and Vulnerability*; Contribution of Working Group II to the Sixth Assessment Report of the Intergovernmental Panel on Climate Change; Pörtner, H.-O., Roberts, D. C., Tignor, M. M. B., Poloczanska, E. S., Mintenbeck, K., Alegría, M., Craig, M., Langsdorf, S., Löschke, S., Möller, V., Okem, A., Rama, B., Eds.; Cambridge University Press: Cambridge, U.K., 2022; pp 1929−2042.

(2) Burdyny, T.; Smith, W. A. CO2 Reduction on Gas-Diffusion Electrodes and Why Catalytic Performance Must Be Assessed at Commercially-Relevant Conditions. *Energy Environ. Sci.* **2019**, *12* (5), 1442−1453.

(3) Stephens, I. E. L.; Chan, K.; Bagger, A.; Boettcher, S. W.; Bonin, J.; Boutin, E.; Buckley, A. K.; Buonsanti, R.; Cave, E. R.; Chang, X.;

Chee, S. W.; da Silva, A. H. M.; de Luna, P.; Einsle, O.; Endrődi, B.; Escudero-Escribano, M.; Ferreira de Araujo, J. V.; Figueiredo, M. C.; Hahn, C.; Hansen, K. U.; Haussener, S.; Hunegnaw, S.; Huo, Z.; Hwang, Y. J.; Janáky, C.; Jayathilake, B. S.; Jiao, F.; Jovanov, Z. P.; Karimi, P.; Koper, M. T. M.; Kuhl, K. P.; Lee, W. H.; Liang, Z.; Liu, X.; Ma, S.; Ma, M.; Oh, H.-S.; Robert, M.; Cuenya, B. R.; Rossmeisl, J.; Roy, C.; Ryan, M. P.; Sargent, E. H.; Sebastián-Pascual, P.; Seger, B.; Steier, L.; Strasser, P.; Varela, A. S.; Vos, R. E.; Wang, X.; Xu, B.; Yadegari, H.; Zhou, Y. 2022 Roadmap on Low Temperature Electrochemical CO2 Reduction. *J. Phys. Energy* **2022**, *4* (4), 042003.

(4) Jouny, M.; Luc, W.; Jiao, F. High-Rate Electroreduction of Carbon Monoxide to Multi-Carbon Products. *Nat. Catal.* **2018**, *1* (10), 748−755.

(5) Ozden, A.; Wang, Y.; Li, F.; Luo, M.; Sisler, J.; Thevenon, A.; Rosas-Hernández, A.; Burdyny, T.; Lum, Y.; Yadegari, H.; Agapie, T.; Peters, J. C.; Sargent, E. H.; Sinton, D. Cascade CO2 Electroreduction Enables Efficient Carbonate-Free Production of Ethylene. *Joule* **2021**, *5* (3), 706−719.

(6) Wei, P.; Gao, D.; Liu, T.; Li, H.; Sang, J.; Wang, C.; Cai, R.; Wang, G.; Bao, X. Coverage-Driven Selectivity Switch from Ethylene to Acetate in High-Rate CO2/CO Electrolysis. *Nat. Nanotechnol.* **2023**, *18*, 299.

(7) Ji, Y.; Chen, Z.; Wei, R.; Yang, C.; Wang, Y.; Xu, J.; Zhang, H.; Guan, A.; Chen, J.; Sham, T. K.; Luo, J.; Yang, Y.; Xu, X.; Zheng, G. Selective CO-to-Acetate Electroreduction via Intermediate Adsorption Tuning on Ordered Cu−Pd Sites. *Nat. Catal.* **2022**, *5* (4), 251−258.

(8) Duong, H. P.; Tran, N. H.; Rousse, G.; Zanna, S.; Schreiber, M. W.; Fontecave, M. Highly Selective Copper-Based Catalysts for Electrochemical Conversion of Carbon Monoxide to Ethylene Using a Gas-Fed Flow Electrolyzer. *ACS Catal.* **2022**, *12* (16), 10285−10293.

(9) Xia, R.; Lv, J. J.; Ma, X.; Jiao, F. Enhanced Multi-Carbon Selectivity via CO Electroreduction Approach. *J. Catal.* **2021**, *398*, 185−191.

(10) Jouny, M.; Luc, W.; Jiao, F. General Techno-Economic Analysis of CO2 Electrolysis Systems. *Ind. Eng. Chem. Res.* **2018**, *57* (6), 2165−2177.

(11) Jeng, E.; Jiao, F. Investigation of CO2single-Pass Conversion in a Flow Electrolyzer. *React. Chem. Eng.* **2020**, *5* (9), 1768−1775.

(12) Subramanian, S.; Middelkoop, J.; Burdyny, T. Spatial Reactant Distribution in CO2 electrolysis: Balancing CO2 utilization and Faradaic Efficiency. *Sustain. Energy Fuels* **2021**, *5* (23), 6040−6048.

(13) Zhang, T.; Bui, J. C.; Li, Z.; Bell, A. T.; Weber, A. Z.; Wu, J. Highly Selective and Productive Reduction of Carbon Dioxide to Multicarbon Products via in Situ CO Management Using Segmented Tandem Electrodes. *Nat. Catal.* **2022**, *5* (3), 202−211.

(14) Storck, A.; Coeuret, A. Mass and Momentum Transfer At a Wall in the Presence of Turbulence Promoters. *Electrochim. Acta* **1977**, *22*, 1155−1160.

(15) Czarnetzki, L. R.; Janssen, L. J. J. Electrode Current Distribution in a Hypochlorite Cell. *J. Appl. Electrochem.* **1989**, *19*, 630−636.

(16) Brown, C. J.; Pletcher, D.; Walsh, F. C.; Hammond, J. K.; Robinson, D. Local Mass Transport Effects in the FMO1 Laboratory Electrolyser. *J. Appl. Electrochem.* **1992**, *22*, 613−619.

(17) Biswas, I.; Sánchez, D. G.; Schulze, M.; Mitzel, J.; Kimmel, B.; Gago, A. S.; Gazdzicki, P.; Friedrich, K. A. Advancement of Segmented Cell Technology in Low Temperature Hydrogen Technologies. *Energies* **2020**, *13* (9), 2301.

(18) Phillips, A.; Ulsh, M.; Porter, J.; Bender, G. Utilizing a Segmented Fuel Cell to Study the Effects of Electrode Coating Irregularities on PEM Fuel Cell Initial Performance. *Fuel Cells* **2017**, *17* (3), 288−298.

(19) Kas, R.; Star, A. G.; Yang, K.; Van Cleve, T.; Neyerlin, K. C.; Smith, W. A. Along the Channel Gradients Impact on the Spatioactivity of Gas Diffusion Electrodes at High Conversions during CO2 Electroreduction. *ACS Sustain. Chem. Eng.* **2021**, *9* (3), 1286−1296.

(20) Wheeler, D. G.; Mowbray, B. A. W.; Reyes, A.; Habibzadeh, F.; He, J.; Berlinguette, C. P. Quantification of Water Transport in a CO2 electrolyzer. *Energy Environ. Sci.* **2020**, *13* (12), 5126−5134.

(21) Iglesias van Montfort, H.-P.; Burdyny, T. Mapping Spatial and Temporal Electrochemical Activity of Water and CO2 Electrolysis on Gas-Diffusion Electrodes Using Infrared Thermography. *ACS Energy Lett.* **2022**, *7* (8), 2410−2419.

(22) Yang, X.-G.; Burke, N.; Wang, C.-Y.; Tajiri, K.; Shinohara, K. Simultaneous Measurements of Species and Current Distributions in a PEFC under Low-Humidity Operation. *J. Electrochem. Soc.* **2005**, *152* (4), A759.

(23) Engl, T.; Langer, M.; Freund, H.; Rubin, M.; Dittmeyer, R. Tap Reactor for Temporally and Spatially Resolved Analysis of the CO2Methanation Reaction. *Chem.-Ing.-Technol.* **2023**, *95*, 658−667.

(24) Chen, Y.; Vise, A.; Klein, W. E.; Cetinbas, F. C.; Myers, D. J.; Smith, W. A.; Deutsch, T. G.; Neyerlin, K. C. A Robust, Scalable Platform for the Electrochemical Conversion of CO2 to Formate: Identifying Pathways to Higher Energy Efficiencies. *ACS Energy Lett.* **2020**, *5* (6), 1825−1833.

(25) Ghanbarian, A.; Kermani, M. J.; Scholta, J.; Abdollahzadeh, M. Polymer Electrolyte Membrane Fuel Cell Flow Field Design Criteria − Application to Parallel Serpentine Flow Patterns. *Energy Convers. Manag.* **2018**, *166*, 281−296.

(26) Park, A. M.; Owczarczyk, Z. R.; Garner, L. E.; Yang-Neyerlin, A. C.; Long, H.; Antunes, C. M.; Sturgeon, M. R.; Lindell, M. J.; Hamrock, S. J.; Yandrasits, M.; Pivovar, B. S. Synthesis and Characterization of Perfluorinated Anion Exchange Membranes. *ECS Trans.* **2017**, *80* (8), 957−966.

(27) Gao, J.; Zhang, H.; Guo, X.; Luo, J.; Zakeeruddin, S. M.; Ren, D.; Grätzel, M. Selective C-C Coupling in Carbon Dioxide Electroreduction via Efficient Spillover of Intermediates As Supported by Operando Raman Spectroscopy. *J. Am. Chem. Soc.* **2019**, *141* (47), 18704−18714.

(28) Wagner, F. T.; Moylan, T. E.; Schmieg, S. J. Hydrophillic Versus Hydrophobic Coadsorption: Carbon Monoxide And Water On Rh(Lll) Versus Pt(Lll). *Surf. Sci.* **1988**, *195*, 403−428.

(29) Baker, D. R.; Caulk, D. A.; Neyerlin, K. C.; Murphy, M. W. Measurement of Oxygen Transport Resistance in PEM Fuel Cells by Limiting Current Methods. *J. Electrochem. Soc.* **2009**, *156* (9), B991.

(30) Kim, C.; Bui, J. C.; Luo, X.; Cooper, J. K.; Kusoglu, A.; Weber, A. Z.; Bell, A. T. Tailored Catalyst Microenvironments for CO2 Electroreduction to Multicarbon Products on Copper Using Bilayer Ionomer Coatings. *Nat. Energy* **2021**, *6* (11), 1026−1034.

(31) Will, F. G.; BenDaniel, D. J. Significance of Electrolyte Films for Performance of Porous Hydrogen Electrodes: I. Film Model. *J. Electrochem. Soc.* **1969**, *116* (7), 933.

(32) Bohra, D.; Chaudhry, J. H.; Burdyny, T.; Pidko, E. A.; Smith, W. A. Modeling the Electrical Double Layer to Understand the Reaction Environment in a CO2 Electrocatalytic System. *Energy Environ. Sci.* **2019**, *12* (11), 3380−3389.

(33) Röhe, M.; Botz, A.; Franzen, D.; Kubannek, F.; Ellendorff, B.; Öhl, D.; Schuhmann, W.; Turek, T.; Krewer, U. The Key Role of Water Activity for the Operating Behavior and Dynamics of Oxygen Depolarized Cathodes. *ChemElectroChem.* **2019**, *6* (22), 5671−5681.

(34) Angulo, A.; van der Linde, P.; Gardeniers, H.; Modestino, M.; Fernandez Rivas, D. Influence of Bubbles on the Energy Conversion Efficiency of Electrochemical Reactors. *Joule* **2020**, *4* (3), 555−579.

(35) Subramanian, S.; Yang, K.; Li, M.; Sassenburg, M.; Abdinejad, M.; Irtem, E.; Middelkoop, J.; Burdyny, T. Geometric Catalyst Utilization in Zero-Gap CO2 Electrolyzers. *ACS Energy Lett.* **2023**, *8* (1), 222−229.

(36) Leonard, M. E.; Orella, M. J.; Aiello, N.; Román-Leshkov, Y.; Forner-Cuenca, A.; Brushett, F. R. Flooded by Success: On the Role of Electrode Wettability in CO2 Electrolyzers That Generate Liquid Products. *J. Electrochem. Soc.* **2020**, *167* (12), 124521.

(37) Hudkins, J. R.; Wheeler, D. G.; Peña, B.; Berlinguette, C. P. Rapid Prototyping of Electrolyzer Flow Field Plates. *Energy Environ. Sci.* **2016**, *9* (11), 3417−3423.

https://doi.org/10.1021/acsenergylett.3c01489
ACS Energy Lett. 2023, 8, 3811−3819

(38) Fenwick, A. Q.; Welch, A. J.; Li, X.; Sullivan, I.; DuChene, J. S.; Xiang, C.; Atwater, H. A. Probing the Catalytically Active Region in a Nanoporous Gold Gas Diffusion Electrode for Highly Selective Carbon Dioxide Reduction. *ACS Energy Lett.* **2022**, *7* (2), 871−879.
(39) Kong, Y.; Liu, M.; Hu, H.; Hou, Y.; Vesztergom, S.; Gálvez-Vázquez, M. de J.; Zelocualtecatl Montiel, I.; Kolivoška, V.; Broekmann, P. Cracks as Efficient Tools to Mitigate Flooding in Gas Diffusion Electrodes Used for the Electrochemical Reduction of Carbon Dioxide. *Small Methods* **2022**, *6* (9), 2200369.
(40) Garcia de Arquer, F. P.; Dinh, C.-T.; Ozden, A.; Wicks, J.; McCallum, C.; Kirmani, A. R.; Nam, D.-H.; Gabardo, C.; Seifitokaldani, A.; Wang, X.; Li, Y. C.; Li, F.; Edwards, J.; Richter, L. J.; Thorpe, S. J.; Sinton, D.; Sargent, E. H. CO2 Electrolysis to Multicarbon Products at Activities Greater than 1 A Cm−2. *Science* **2020**, *367* (6478), 661−666.
(41) Xu, Q.; Xu, A.; Garg, S.; Moss, A. B.; Chorkendorff, I.; Bligaard, T.; Seger, B. Enriching Surface-Accessible CO2 in the Zero-Gap Anion-Exchange-Membrane-Based CO2 Electrolyzer. *Angew. Chem., Int. Ed.* **2023**, *62* (3), e202214383.
(42) Hou, J.; Chang, X.; Li, J.; Xu, B.; Lu, Q. Correlating CO Coverage and CO Electroreduction on Cu via High-Pressure in Situ Spectroscopic and Reactivity Investigations. *J. Am. Chem. Soc.* **2022**, *144* (48), 22202−22211.
(43) Hansen, K. U.; Cherniack, L. H.; Jiao, F. Voltage Loss Diagnosis in CO2 Electrolyzers Using Five-Electrode Technique. *ACS Energy Lett.* **2022**, *7* (12), 4504−4511.

https://doi.org/10.1021/acsenergylett.3c01489
ACS Energy Lett. 2023, 8, 3811−3819